Correlations between the magnetic and structural properties of Ca-doped $BiMnO_3$

H. Woo,[1] T. A. Tyson,[1] M. Croft,[2] S-W. Cheong,[2,3] and J. C. Woicik[4]
[1]*Department of Physics, New Jersey Institute of Technology, Newark, New Jersey 07102*
[2]*Department of Physics, Rutgers University, Piscataway, New Jersey 08855*
[3]*Bell Laboratories, Lucent Technologies, Murray Hill, New Jersey 07974*
[4]*National Institute of Standards and Technology, Gaithersburg, Maryland 20899*
(Received 20 June 2000; published 6 March 2001)

The $Bi_{1-x}Ca_xMnO_3$ system is known to exhibit charge ordering for a much broader range of x than the $La_{1-x}Ca_xMnO_3$ system. However, the properties of $Bi_{1-x}Ca_xMnO_3$ over the entire doping range are not well understood. We have performed magnetization and resistivity measurements as well as x-ray absorption and x-ray diffraction measurements on $Bi_{1-x}Ca_xMnO_3$ to correlate structural, magnetic, and transport properties. The system is insulating and antiferromagnetic for the entire range of x studied ($x \geqslant 0.4$) except near $x \sim 0.9$, where we find a canted spin arrangement with approximately one Bohr magneton per Mn site. Detailed magnetization measurements were performed as a function of field and temperature to explore the net moment on the Mn sites as a function of x and reveal the charge ordering and Néel temperatures. X-ray absorption measurements reveal significant structural distortions of the Mn-O bond distributions with increasing Bi content that correlates directly with increasing charge-ordering temperatures. Moreover, the x-ray diffraction data reveal peak splittings consistent with lower-symmetry cells as Bi content increases. These structural-magnetic correlations point to the importance of Mn-O distortions in stabilizing the charge-ordered state in the manganites.

DOI: 10.1103/PhysRevB.63.134412 PACS number(s): 75.30.Vn, 78.70.Dm, 75.70.Pa, 61.10.Ht

I. INTRODUCTION

As a function of temperature, pressure, doping, and A^{3+}/A'^{2+}-site ionic radius, perovskite mixed-valent manganites $A^{3+}_{1-x}A'^{2+}_{x}MnO_3$ (e.g., A^{3+}=Bi, La, Pr, Nd, etc. and A'^{2+}=Ca, Sr, Ba, Pb, etc.) show intriguing properties such as structural transformations, charge ordering (CO), metal-insulator transitions, and magnetic ordering [ferromagnetic (FM)-antiferromagnetic (AF)] transformations.[1–4] In addition to the rich basic physics exhibited by these materials, there is also much interest from the technological perspective in these materials because they are known to exhibit ''colossal'' magnetoresistance (CMR).[5]

The phase diagram of the prototypical $La_{1-x}Ca_xMnO_3$ (LCMO) system is well documented, and extensive structural, magnetic, and transport measurements have been performed.[1,9] For $0<x<\sim 0.21$, the system is an insulator (I) with a canted antiferromagnetic (CAF) or ferromagnetic ground state. For the range $\sim 0.21<x<0.5$, a ferromagnetic metallic (FM) ground state occurs that undergoes a coincident metal-to-insulator (MI) and FM-to-paramagnetic (PM) transformation on the temperature scale 150–250 K.[2,6,7] In the $0.50<x<0.875$ region, the materials are insulators with a charge/orbital-ordered (*CO* ordered) and AF-ordered ground state, which, upon elevating the temperature, first loses its AF ordering (at T_N) and then, at a higher temperature (T_{CO}), its *CO* ordering.[8]

$Bi_{1-x}Ca_xMnO_3$ (BCMO) constitutes a very interesting but less-studied system. Early experiments showed that the system is insulating over a broad region of Ca doping $0.2<x<1.0$.[10] In addition, strong charge ordering has been observed in neutron-scattering measurements for $x \sim 0.8$.[4,14] The $x=0$ end member was found to be ferromagnetic with a moment per Mn approaching the theoretical maximum. These intriguing properties, contrasted with those of the LCMO system, make this system ideal for understanding the correlations between structure, transport, and magnetic properties in manganite materials.

In this work we first draw together structural, magnetic, and resistivity results, both from the literature and from work in our group, into an overall phase diagram for the BCMO system for $0.4 \leqslant x \leqslant 1.0$. We then focus on systematic x-ray absorption spectroscopy (XAS) measurements of the BCMO materials. Despite substantial disparities with other more-studied systems, the continuous Bi-induced stabilization of the Mn^{3+} state is demonstrated with Mn-K near-edge XAS measurements. Both near-edge and extended x-ray absorption fine-structure (EXAFS) XAS measurements provide direct evidence of significant local distortions accompanying increasing Bi content in this system.

II. PREVIOUS WORK ON $Bi_{1-x}Ca_xMnO_3$

A large, but somewhat scattered, body of work has been performed on the doped BCMO system. This work is summarized in this section.

Bokov, Grigoryan, and Bryzhina[10] studied the structural, magnetic, and resistivity properties of the BCMO system for $0.2 \leqslant x \leqslant 1.0$. Their phases included two monoclinic phases and one orthorhombic phase as a function of temperature for $x<0.4$; one of the monoclinic phases disappears for x above ~ 0.4, for $0.4 \leqslant x \leqslant 0.83$ a high-temperature cubic phase transforms to a monoclinic low-temperature phase, and above $x \sim 0.83$ the more distorted monoclinic phase gives rise to a higher-symmetry orthorhombic phase. Their magnetic measurements showed a FM-like Curie constant (θ) at

 ©2001 The American Physical Society

high temperatures for all $x<0.9$.

Chiba *et al.*[11,13] contrasted the magnetic, electrical, and magnetoresistance properties of $(Bi,AE)MnO_3$ ($AE=Ca, Sr$) with those of LCMO in the highly doped $x\geqslant 0.8$ regime. They noted that while the Bi- and Ca-based systems had the same crystal symmetry and weak ferromagnetism in this Ca-rich region, the magnetic moments in the Bi system were larger than those in the La system at the same Ca content. $CaMnO_3$ was found to exhibit semiconductor-type and antiferromagnetic behavior.[12] Chiba *et al.*[11] found that the low-temperature resistivity drops continuously when $CaMnO_3$ is doped with Bi^{3+} (electron doping) and reaches minimum resistivity at $x=0.875$ with a weak temperature dependence. At $x=0.85$ (also $x=0.8$), a sharp increase in magnetization with increasing temperature was found, which suggests anomalous magnetic transition temperatures. The Néel temperature was found to be almost constant for $0.875\leqslant x\leqslant 0.95$, while the paramagnetic Curie temperature decreased with increasing Ca doping. At $x=0.875$, the Néel temperature approaches the paramagnetic Curie temperature and a maximum saturation magnetization of $1.1\mu_B$ per Mn site is obtained—this is about $\frac{1}{3}$ of the fully aligned value of $3.1\mu_B$, suggesting spin canting.

Cheong and Hwang expanded on the magnetic phase diagram of Chiba *et al.* by studying the charge-ordered phases for $0.5<x<0.7$.[9] For this range, the charge-ordering temperature is always above 300 K. The maximum charge-ordering temperature of 332 K was found to occur at $x\sim 0.63$; the same behavior of the charge-ordering temperature was observed in the LCMO system.

Bao *et al.*[4] performed neutron-scattering, electron-diffraction, and bulk magnetic measurements on single-crystal BCMO ($0.74\leqslant x\leqslant 0.82$). For $x=0.82$, a structural transition was found at the charge-ordering temperature $T_{CO}=210$ K in which the lattice parameters changed abruptly. This coincides with the transition from orthorhombic to monoclinic *II* found by Bokov, Grigoryan, and Bryzhina.[10] Above T_{CO} ferromagnetic spin fluctuations were found by neutron diffraction. These fluctuations switch over to antiferromagnetic fluctuations below T_{CO}. Strong competition between FM double-exchange charge ordering and AF superexchange occurs in this system. The Néel temperature was found to be 160 K. The same trends were also found in earlier neutron-diffraction measurements by Turkevich and Plakhtii[14] on $Bi_{0.15}Ca_{0.85}MnO_3$. They found the signature of the onset of antiferromagnetic Mn-Mn interactions at low temperatures as evidenced by appearance of {110} and {211} superstructure lines.

Optical conductivity measurements by Liu, Cooper, and Cheong[15] divide the phase diagram of this system into three distinct temperature regions. For $T>T_{CO}$ ferromagnetic correlations exist, for $T_N<T<T_{CO}$ phase separation into CO-(AF) and ferromagnetic regions coexists, and for $T<T_N$ a charge gap develops, and a long-range antiferromagnetism is observed.

Murakami *et al.*[16] found evidence for charge ordering in $Bi_{0.2}Ca_{0.8}MnO_3$ concomitant with 32- and 36-fold periodicity. The charge-ordering temperature T_{CO} was found to be $\sim$160 K and below T_{CO}, the magnetic structure was transformed from a paramagnetic to an antiferromagnetic phase. Long-period structures with 32- and 36-fold periodicity associated with charge ordering in $Bi_{0.2}Ca_{0.8}MnO_3$ were found.

Utilizing high-pressure synthesis, Sugawara and Iida[17] obtained the end member $BiMnO_3$. It was found that unlike $LaMnO_3$, $BiMnO_3$ is ferromagnetic with a Curie temperature of 103 K. The saturation magnetization was observed to be $\sim 4\mu_B$ per Mn site. A distorted perovskite structure with a triclinic pseudounit cell was found.

Recently, Atou *et al.*[18] reported powder-neutron-diffraction measurements of the structure of the ferromagnetic perovskite $BiMnO_3$ formed under high pressure. A distorted perovskite structure was found with monoclinic $C2$ space-group symmetry. They suggested that the distortions were caused by the polarized Bi-$6s^2$ lone pairs.[19] The combined Jahn-Teller instability of Mn^{3+} and lone pair-induced distortions result in a highly disordered $BiMnO_3$ system with a range of Mn-O bonds between 1.78 and 2.32 Å. The origin of the ferromagnetic tendency is uncertain.

Recently, Ohshima *et al.*[20] prepared films of $BiMnO_3$ on $SrTiO_3$ substrates. Although the films (200–1200 Å) exhibited the ferromagnetic behavior seen in the corresponding bulk material, the saturation moment of the thick films fell short ($M=2.8\mu_B$) of the bulk value ($M=3.6\mu_B$). In addition, a strong dependence of the saturation moment on film thickness was found. Also, unlike the bulk material, strong hysteresis was found in the film samples.

The broad array of interesting properties suggests a deep correlation between the long-range and local structure, and the magnetic and transport trends in the BCMO system.

III. EXPERIMENTAL METHODS

We have prepared a series of BCMO ($x\geqslant 0.4$) polycrystalline samples using the standard solid-state reaction method. Stoichiometric mixtures of Bi_2O_3, $CaCO_3$, and MnO_2 were mixed, ground, and pressed into pellets, which were calcined at 900 °C. After calcination, the samples were reground and sintered at 1000 °C in air. This was repeated one more time. $BiMnO_3$ was synthesized under high pressure (25 kbar) at 800 °C by using a cylinder-piston-type pressure furnace. The purity of $BiMnO_3$ was checked by x-ray fluorescence spectroscopy.

Magnetization, resistivity, x-ray diffraction, and x-ray absorption measurements were performed. Magnetic measurements were performed using a superconducting quantum-interference device magnetometer. The standard four-probe method was used for resistivity measurement. X-ray diffraction (XRD) measurements were carried out using a x-ray diffractometer with a liquid-nitrogen-cooled Li-drifted germanium detector and Cu-K_α radiation. Lattice parameters were extracted using DICVOL and ITO software packages.[21]

X-ray-absorption spectra were measured at Brookhaven National Laboratory's National Synchrotron Light Source beam lines X11A, X18B, X19A, and X23A2. Si(111) monochromator crystals were used on X18B and X19A while Si(311) crystals were used on X23A2. Spectra were taken in

transmission mode using N_2-filled ion chambers. The reduction of the x-ray absorption measurements was performed using standard procedures.[22] Calibration was accomplished by defining the first inflection point in a simultaneous Mn foil as 6539 eV, the ionization threshold. Consistency between different beamlines was checked by using a MnO_2-powder reference sample over the complete data range.

The background and signal extraction was carried out using AUTOBK.[23] The fine-structure signals were extracted from the spectra as the difference between the normalized spectra and an adjustable spline function fit through the post-edge region normalized by the absorbance decrease with energy, the parameters of which were adjusted to minimize low-frequency residuals in the Fourier transform. After comparison, two to ten individual scans were averaged. Representative data are given in the inset in Fig. 10. Information about the Mn-O bond distributions was obtained by fitting the k^3 weighted raw data over the range $2<k<12.3\,\text{Å}^{-1}$ [$k=\sqrt{(2m/\hbar^2)(E-E_0)}$]. Fitting was made using the functional form

$$\chi_{\text{model}}(k)=\sum_{i}^{\text{shells}} S_0^2\frac{N_i}{kR_i^{2i}}f_i(\pi,k,R_i)\exp(-2\sigma_i^2k^2+\tfrac{2}{3}C_{4i}k^4)\times\sin[2kR_i-\tfrac{4}{3}C_{3i}k^3+\phi_i(\pi,k,R_i)], \quad (1)$$

where S_0^2 is the scale factor for the multielectron effects, N_i is the coordination number of the i shell, R_i is the radius of the i shell, σ^2 is the mean-square radial displacement or Debye-Waller factor, f_i is the backscattering amplitude of the photoelectron due to the atoms of the i coordination shell, C_3 and C_4 are cumulants[24,25] of a distribution to model anharmonic effects and/or non-Gaussian disorder,[25,26] respectively, and ϕ_i is the phase shift.

The inhomogeneously broadened (fine structure) χ based on the statistical ensemble of scattering path lengths[27] is written as

$$\langle\chi(k;R)\rangle=\int dR\,P(R)\chi(k;R). \quad (2)$$

In the cumulant approach to distributions one represents the Fourier transform of a distribution by its moments. For small deviations from Gaussian distribution a rapidly converging series makes possible a description by a small number of parameters. For the effective distribution we have

$$\ln\int_0^\infty P(r,\lambda)e^{2ikr}\,dr=C_0+\sum_{n=1}^{\infty}\frac{(2ik)^n}{n!}C_n, \quad (3)$$

where

$$P(r,\lambda)=\rho(r)\frac{e^{-2r/\lambda}}{r^2}.$$

The leading cumulants (C_n) are

$$C_1=\langle R\rangle,$$

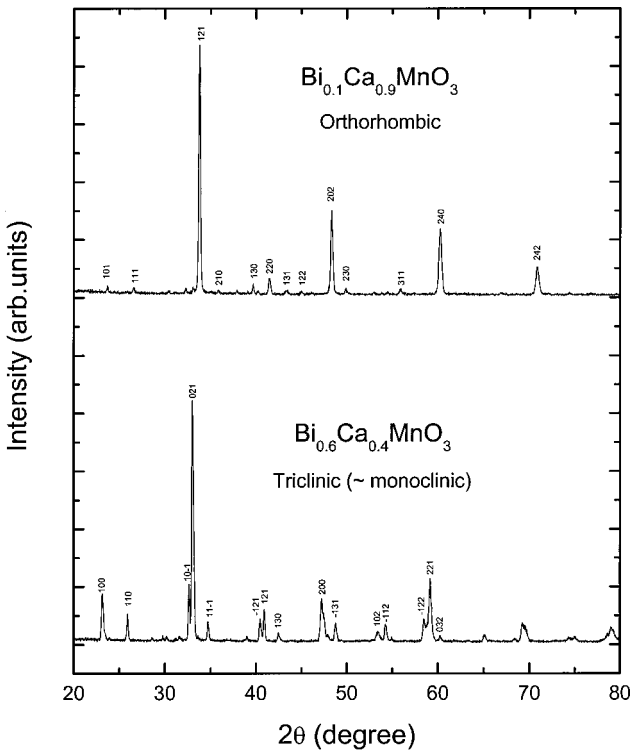

FIG. 1. Powder x-ray-diffraction curves for $x=0.4$ and 0.9. The splitting and broadening of the $x=0.4$ peaks are indicative of a lower space-group symmetry. The region above 60°($=2\theta$) for the $x=0.4$ pattern manifests closely spaced multiple reflections and the indices have been omitted.

$$C_2=\sigma^2=\langle R^2\rangle-\langle R\rangle^2,$$

$$C_3=\langle R^3\rangle-3\langle R^2\rangle\langle R\rangle+2\langle R\rangle^3,$$

$$C_4=\langle R^4\rangle-4\langle R^3\rangle\langle R\rangle-3\langle R^2\rangle^2+12\langle R^2\rangle\langle R\rangle^2-6\langle R\rangle^4. \quad (4)$$

For an effective Gaussian distribution, cumulants (C_n) higher than the second vanish. In a convergent series the C_3 and C_4 parameters are related to asymmetry and flatness of the distribution, respectively [see Eq. (4)]. We performed fits with parameters up to C_4. Photoelectron scattering factors utilized in these fits were obtained using the code FEFF7.[28] These complex phase shifts included the electron damping. By defining the coordination numbers N as the values known for perovskite systems, average bond lengths R and Debye-Waller factors σ were extracted from the fits as well as C_3 and C_4 for the Mn-O (first-shell) bond distribution. The errors in these parameters were estimated based on the statistical spread found for fits to individual scans.

IV. RESULTS AND DISCUSSION

A. X-ray-diffraction measurements

Figure 1 shows representative room-temperature x-ray diffraction profiles for the $x=0.4$ and 0.9 materials. The $x=0.9$ material was indexed with the orthorhombic ($\alpha=\beta=\gamma=90°$) perovskite structure and the extracted lattice parameters were $a=5.314$, $b=7.480$, and $c=5.297$ Å. On the

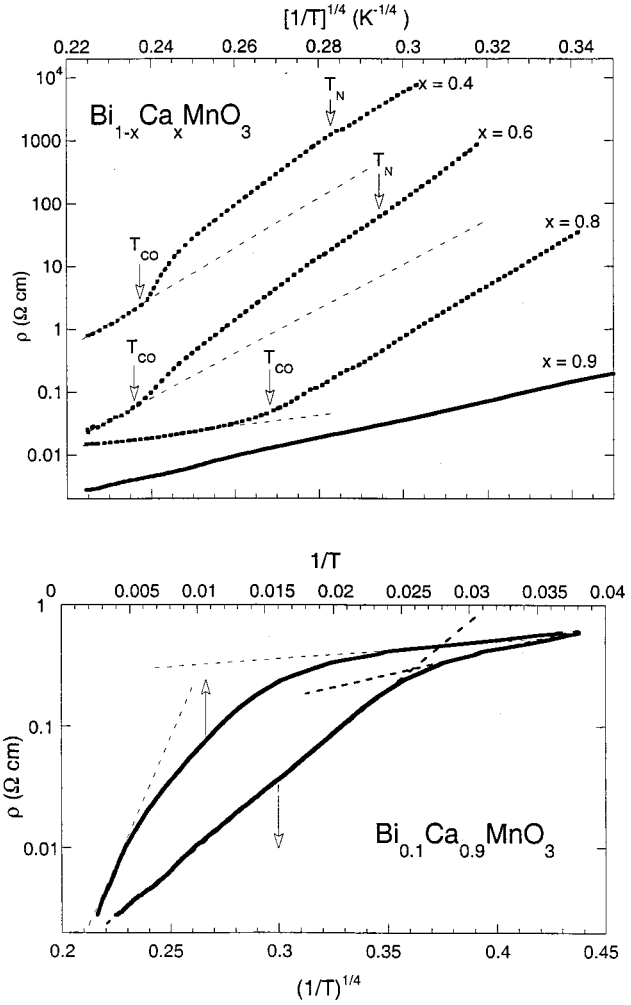

FIG. 2. Temperature dependence $[1/T^4(K^{-4})]$ of the electric resistivity for $x=0.4$, 0.6, 0.8, and 0.9, respectively. Note that there are anomalies at $T_{CO}=315$, 330, and 190 K for $x=0.4$, 0.6, and 0.8, respectively. $T_N=160$ and 130 K for $x=0.4$ and 0.6, respectively. In the lower panel we compare the logarithmic resistivity variation for the $x=0.9$, $Bi_{1-x}Ca_xMnO_3$ material plotted versus $1/T$ (upper curve) and $1/T^{1/4}$ (lower curve).

other hand, the $x=0.4$ pattern was indexed with a triclinic (nearly monoclinic) cell with the structural parameters of $a=3.848$, $b=7.655$, and $c=3.855$ Å, $\alpha=90.166$, $\beta=90.877$, and $\gamma=89.997°$. This is consistent with the splitting of the *a*, *b*, and *c* lattice parameters founded by Bokov, Grigoryan, and Bryzhina.[10] The $x=0.6$ exhibited a similar triclinic structure but with the triclinic splittings much reduced. The $x=0.8$ assumes a structure with lattice parameters similar to that for $x=0.9$. Hence, reduced Ca content coincides with reduced space-group symmetry.

B. Resistivity measurements

We performed resistivity measurements for $x=0.4$, 0.6, 0.8, and 0.9 (see Fig. 2, top panel). The BCMO system is insulating for $x\geqslant 0.4$ except near $x\sim 0.9$. We noticed that the resistivity curves jump at the charge-ordering temperatures (T_{CO}) at 315, 330, and 190 K for $x=0.4$, 0.6, and 0.8, respectively. At the Néel temperature the $x=0.4$ sample shows a little dip indicating phase transition.

Zeng, Greenblatt, and Croft[29] have reported an activated variation of the resistivity $[\rho=\rho_O e_e^{T_0/T}]$ with $T_0=778$ K and $\rho_O=12.3\,\Omega$ cm for $CaMnO_3$. In the bottom of Fig. 2 we compare the logarithmic resistivity variation for the $x=0.9$, BCMO material plotted versus $(1/T)$ and $(1/T)^{1/4}$. Unlike the pure $x=0.0$ system, the strong curvature of the $x=0.9$ material in the $1/T$ plot indicates that (i) its resistivity cannot be characterized as activated, and (ii) a simple crossover between two activation regions appears untenable. On the other hand the $(1/T)^{1/4}$ plot manifests a wide range of high-temperature linearity crossing over rather sharply to a low-temperature linear range. Fitting the data to the form $[\rho=\rho_O\exp(T_0/T)^{1/4}]$ yields T_0 and ρ_O values of 1.42 MK and 1.19 $\mu\Omega$ cm at higher temperatures and 5470 K and 0.0136 Ω cm at lower temperatures.

As discussed below, at high temperatures these doped manganites manifest FM correlations. Models of these materials picture the FM correlations as local polarons randomly distributed and fluctuating.[1] In this picture, the carrier hopping between FM fluctuations would involve disordered and potentially variable range hopping. In view of this, Fontcuberta *et al.*[30] used the $(T_0/T)^{1/4}$ dependence of the log of the resistivity data to characterize manganite system results. Varma[31] argued in favor of a $(T_0T)^{1/2}$-type behavior for manganite systems due to the importance of electron interactions in the localization. This provides some motivation for trying the three-dimensional variable range hopping form $[\rho=\rho_O\exp(T_0/T)^{1/4}]$ as an ansatz for plotting the data. At this juncture, however, we prefer to view the $(1/T)^{1/4}$ display of the data simply as an empirically useful method of characterizing the high-temperature variation of the resistivity.

In Fig. 2 (upper panel) the logarithmic variation of the resistivities of the $x=0.4$, 0.6, 0.8, and 0.9 materials is plotted versus $(1/T)^{1/4}$. In the smaller range of this plot the $x=0.9$ variation is quite linear. The $x=0.4$, 0.6, and 0.8 material resistivities can also be well approximated by a $[\rho=\rho_O\exp(T_0/T)^{1/4}]$ form for $T>T_{CO}$ (the charge/orbital-ordering temperatures). For the high-temperature-region materials the values of ρ_O and T_0 are given by 3.3 nΩ cm, and 53 MK at $x=0.4$; 0.30 nΩ cm, and 43 mK at $x=0.6$; 176 $\mu\Omega$ cm and 0.15 mK at $x=0.8$. The onset of the charge-ordered phase is characterized by a clear increase in the resistivity for all of the materials (see top of Fig. 2). This is consistent with the suppression of the carrier hopping associated with the charge-ordered phase. No clear resistivity anomalies associated with the AF-ordering temperatures (T_N) were observed.

It is worth noting for later reference that the magnitude of the resistivity at 300 K versus composition [see Fig. 3(b)] from our and previous work[11] shows a distinctive dip (of nearly 2.5 orders of magnitude) in the $0.8<x<0.95$ range. A similar drop in the localization energy-scale parameters (T_0) is evident from our data. The low-x side of this dip is associated with the suppression of CO correlations whereas the rise, approaching $CaMnO_3$, is related to the crossover to insulating behavior with the disappearance of doped carriers.

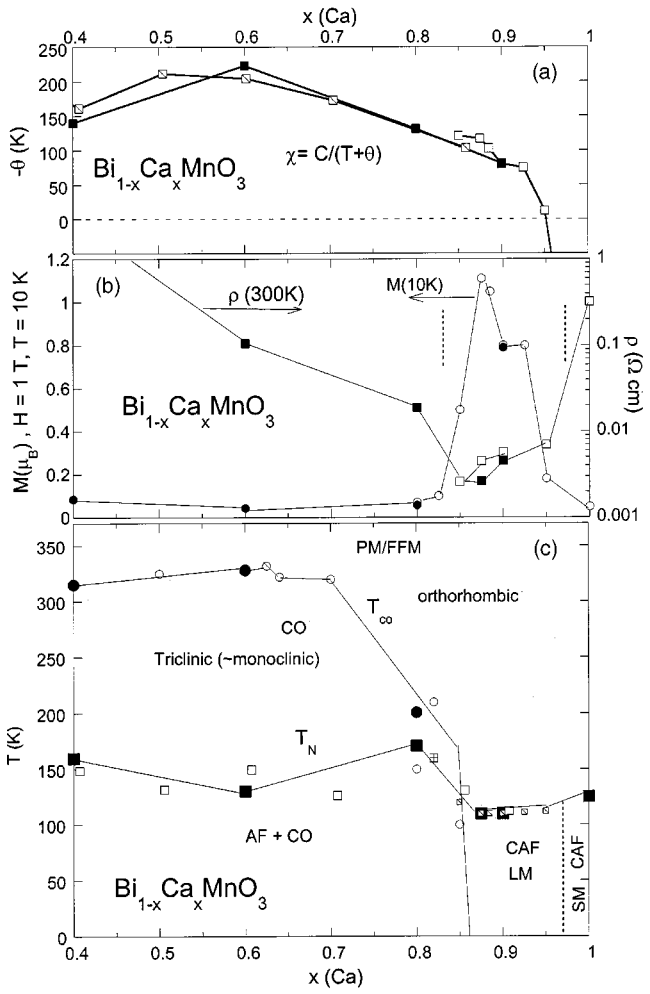

FIG. 3. (a) The high-temperature Curie-Weiss temperature variation versus x in the BCMO system from our work (filled squares) and from that of Chiba *et al.* (open squares) (Ref. 11) and Bokov *et al.* (back-slashed squares) (Ref. 10). Note that the susceptibility θ values from our group [and from Chiba *et al.* (Ref. 11)] were determined for $T<400$ K (in the PM phase) and from Bokov *et al.* (Ref. 10) in the $400\,\mathrm{K}<T<700\,\mathrm{K}$ range. (b) The low-temperature magnetization (at $H=1$ T) and room-temperature resistivity variation versus x in the BCMO system from our work (filled squares and filled circles) and from Chiba *et al.* (open squares and open circles) are presented (Ref. 11). (c) A summary phase diagram of the BCMO system. We indicate phases including the AF ordering temperatures and AF phase, canted AF (CAF) phase with large moment, (LM), canted AF (CAF) phase with small moment (SM), high-temperature range supporting ferromagnetic fluctuations (FMF), charge/orbital-ordered phase, and its ordering temperature. Note that the data comes from our work (filled triangles and filled squares), Chiba *et al.* (open squares and open inverted triangles) (Ref. 11), Bokov *et al.* (back-slashed squares) (Ref. 10), and Bao *et al.* (open triangle with vertical bar and squares with cross) (Ref. 4).

C. Magnetic measurements

Magnetization measurements [see Figs. 4(a)–(d)] were performed with magnetic fields of 1, 2, and 4 T for $x=0.4$, 0.6, and 0.8, and 0.01, 0.1, and 1 T for $x=0.9$. The magnetic susceptibility at the high temperatures showed Curie-Weiss-type behavior $[\chi=C/(T+\theta)]$ with an FM-like (i.e., negative) θ value over the $0.4\leqslant x\leqslant 0.95$ as illustrated in Fig. 3(a). Here the Curie-Weiss behavior is for temperatures above the charge-ordering and antiferromagnetic transition temperatures. Thus this high-temperature range appears to be dominated by local ferromagnetic fluctuations (FMF) that are presumably mediated by Mn^{3+}/Mn^{4+} hopping-induced double exchange interactions. With decreasing temperature our $x=0.4$, 0.6, and 0.8 magnetization curves [see Figs. 4(a)–(d)]

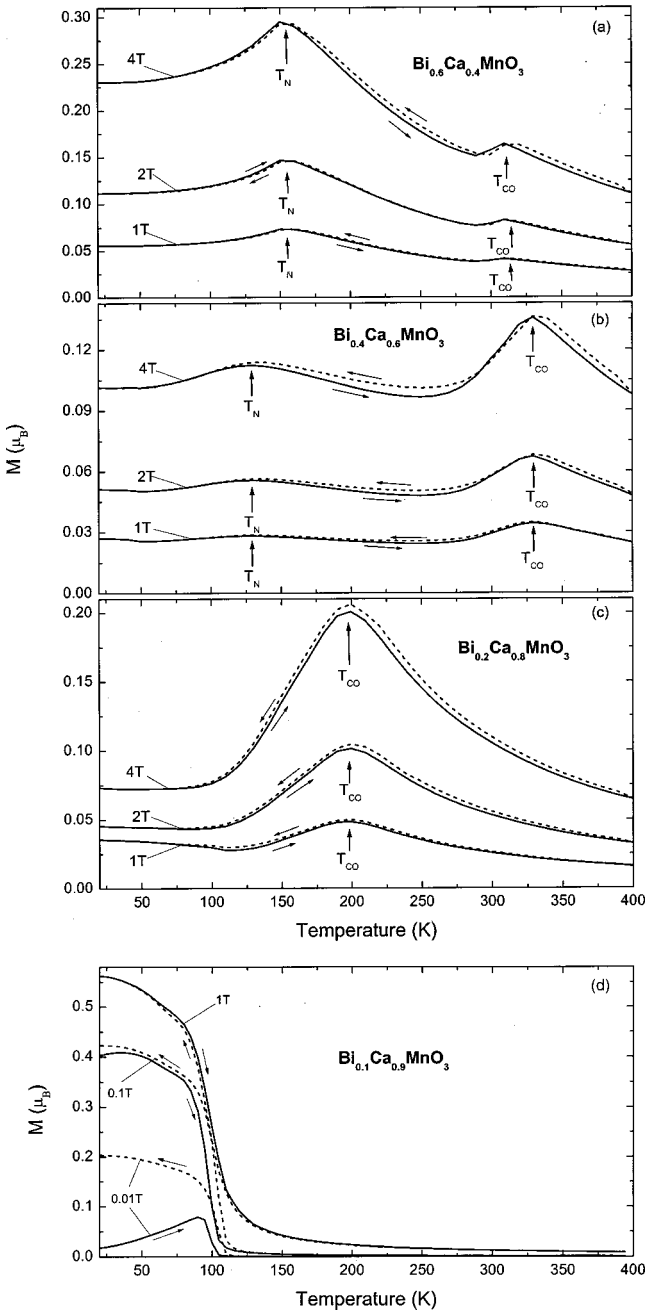

FIG. 4. Temperature dependence of the magnetization for $x=0.4$, 0.6, 0.8, and 0.9 as (a), (b), (c), and (d). The magnetization measurements at $x=0.4$, 0.6, and 0.8 were taken with magnetic fields of 1, 2, and 4 T for cooling down and warming up. For $x=0.9$ measurements were made with magnetic fields at 0.01, 0.1, and 1 T.

exhibit distinct maxima at the charge-ordering temperatures (T_{CO}) indicated. The neutron-scattering results of Bao *et al.*[4] and Turkevich and Plakhtii[14] (on an $x=0.82$ material) have nicely correlated such maxima with the suppression of the FMF when the charge ordering freezes out the hopping mechanism. In the charge-ordered phase, AF superexchange interactions dominate,[4] leading to an AF ordering at a temperature (T_N) in the 129–171 K range. T_N is identified with a lower-temperature local-magnetization maximum. In the $x=0.8$ material the signature of the AF ordering is perceptible only as a subtle shoulder on the low-temperature side of the CO-related peak in the magnetization [see Fig. 4(c)].

The CO phase is suppressed for x values above ~ 0.85. Our $x=0.9$ magnetization curves, for example, reflect the development of a robust net moment, which depends on the field strength, below a magnetic ordering temperature near 110 K. The onset of an AF-type order in this temperature range is common to materials with $0.85<x\leqslant 1.0$ in this system as is the appearance of a net FM moment in a magnetic field. This FM moment has been attributed in the past to FM-interaction induced moment canting. However the magnitude and nonlinear field onset of the FM moment varies strongly in this $0.85<x\leqslant 1.0$ range as illustrated by the $H=1$ T moment variation vs x (from our and other work) in Fig. 3(b).[11] The rapid rise in the FM moment as x increases through 0.85 marks the exit from the CO-AF state. The similarly rapid magnetization drop near $x=0.95$ correlates with the suppression of a FM-θ value (high-T FMF) in the same range. As has been noted previously, the θ value of the $x=1.0$ material is several folds larger than the AF-T_N, suggesting possible low-energy-scale nonmagnetic (covalency) effects in the pure Ca material.

The nonlinear field dependence of the magnetization in $CaMnO_3$ and its response to electron doping has been touched upon (although too briefly) in the literature. The roles of magnetic frustration, AF-domain-spin canting,[29] homogeneous canted antiferromagnetic (CAF) order, and (most recently) local-scale FM/AF coexistence have all been brought up in this regard.[29,32] In Fig. 5 we illustrate a subtle field-dependent behavior in these BCMO materials that may reflect a competing FM component in the CO-AF state of this system.

The M/H curves in Fig. 5 represent the finite field susceptibility (as opposed to the differential susceptibility dM/dH) and help to highlight field-dependent saturation effects in the magnetic response. For the $x=0.9$ material [Fig. 5(d)] the M/H curves at low field (e.g., $H=0.1$ T) manifest a tremendous response at the ordering temperature. The $H=1$ T, M/H curve shows a typical FM component response below T_N and its smaller magnitude simply indicates that the FM response saturated at a much smaller field. This type of behavior is the basis for CAF or locally coexisting FM-AF order proposed for such $x>0.85$ range materials.

In a simple AF system, where the field energy is much less than T_N, the field response should be small and M/H would be expected to increase with increasing field (at least until spin-flop effects saturate). The M/H curves of the $x=0.4$ material in Fig. 5(a) illustrate this type of behavior.

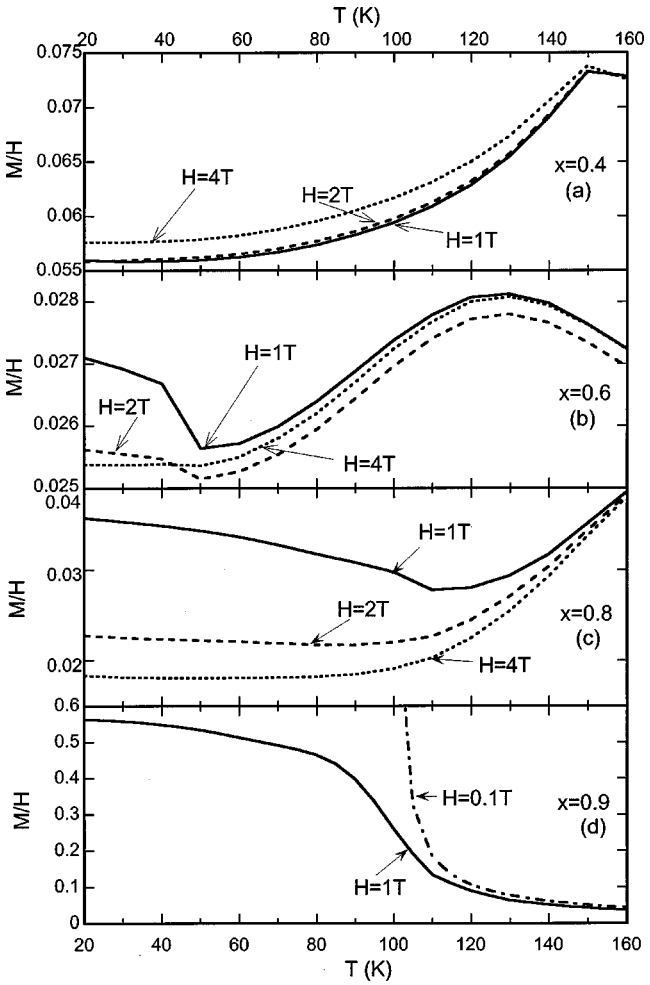

FIG. 5. The finite field susceptibility (M/H) in units of emu·mol^{-1}·T^{-1} in the low-temperature ordered phase of the $x=0.4$, 0.6, 0.8, and 0.9 materials. Note the nonlinear saturation effects that occur in field (see text).

In Fig. 5(c) the M/H curves within the CO-AF phase of the $x=0.8$ material are shown. There is a small but clear nonlinear field response below about 100–120 K in the 1 T curve that is saturated in the higher-field curves. Comparison of Figs. 5(c) and (d) shows that this field effect in the $x=0.8$ material is similar in thermal variation, although much smaller in magnitude, to that in the $x=0.9$ material. Again in the M/H results for $x=0.6$ (Fig. 5) a similar (albeit quite small) low-T low-field increase in the response can be seen. For $x=0.6$ the energy scale for this effect has moved down to about 50 K. If one refers to the 1 T susceptibility results of Chiba *et al.*,[11] one notes the presence of low-temperature FM-moment response in the $x=0.8$ and 0.85 materials in their CO/AF states. Whether these effects are related to local composition fluctuations, CO/AF-domain interface, or FM-like impurity site effects are at present unclear and further work on these effects is warranted.

D. Phase diagram

In Fig. 3 we summarize our results and previous magnetic results for the BCMO system as a phase diagram. Here the

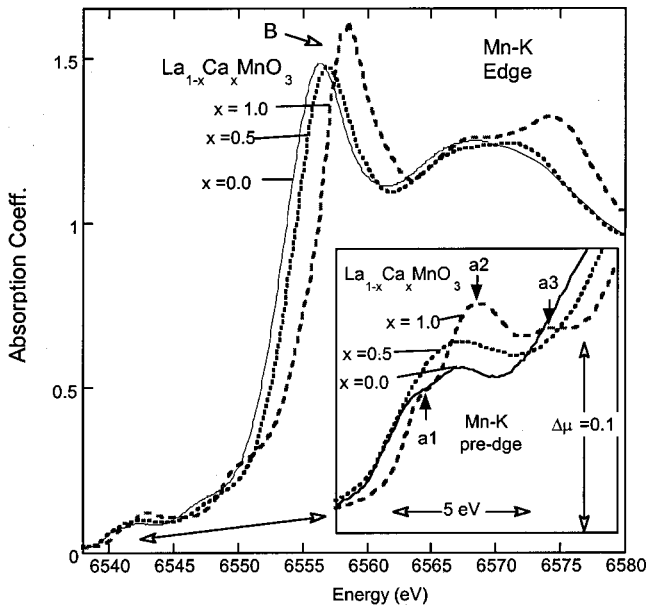

FIG. 6. The Mn-K near-edge spectra for the extensively studied $La_{1-x}Ca_xMnO_3$ system, for $x=0.0$, 0.5, and 1.0.

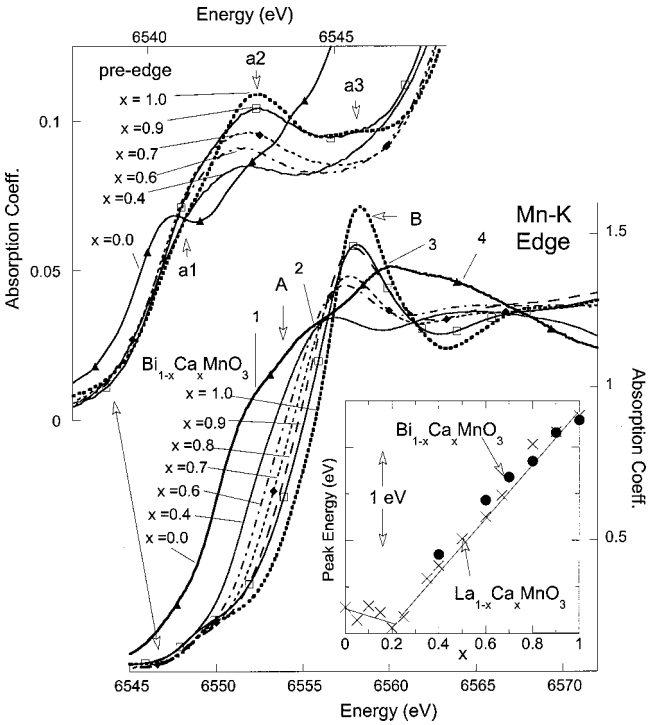

FIG. 7. The Mn-K near-edge spectra showing the evolution in the $Bi_{1-x}Ca_xMnO_3$ system with doping. Note the changes in pre-edge and main-line amplitudes. The inset shows the evolution position of the main line (*B* feature) as a function of *x* in both $Bi_{1-x}Ca_xMnO_3$ (solid circles) and $La_{1-x}Ca_xMnO_3$ (*x*'s) indicating similar changes in valence with doping.

previous work on this system focused either on restricted temperature or composition ranges. Our results augment the previous work and we have carefully attempted to draw together both our and previous results. The high-temperature phase is a paramagnet (PM) with ferromagnetic fluctuations (FMF) for the range $x<0.95$. The loss of FM correlations, approaching the $x=1.0$ (pure-Ca) material is marked by a dotted line. For the $x<0.85$ range the Mn^{3+}-Mn^{4+} hopping, supporting the FMF, is quenched upon crossing a line of charge-ordering transitions (*TCO*). With further cooling, in the $x<0.85$ range, a transformation to an antiferromagnetic (while still CO ordered) ground state occurs below a line of temperatures T_N (in the 110–160 K range).

It is worth noting that the charge-ordered phase of this system is stable over a wider range of compositions and temperatures than in any of the other manganite systems. In the case of the LCMO system, for example, in the $0.4<x<0.5$ range an FM metallic phase has replaced the charge-ordering state found here as the ground state. Moreover, in none of the other systems does the CO ordered state persist above room temperature.

The loss of CO correlations for $x>0.8$ appears to enable the Mn^{3+}/Mn^{4+} hopping and FMF to persist to room temperature and below, as evidenced by a wider FM Curie-Weiss range for the susceptibility and the strongly reduced resistivity in this *x* range. Moreover, an FM component (peaking near $x=0.875$) also appears to be incorporated into the AF ground state in this range as reflected by the magnetization at 10-K variation versus *x* in Fig. 3(c).

E. Mn-K near-edge XAS

Previous work has shown the Mn-K near-edge spectra to be useful in chronicling the Mn-valence/configuration change in the LCMO system.[29] In Fig. 6 the main-edge (and pre-edge in the inset) spectra for $x=0.0$, 0.5, and 1.0 in this system are shown. It should be noted that the peak feature *B* shifts markedly between the formally Mn^{3+} and Mn^{4+} compounds with $x=0.0$ and 1.0; the $x=0.5$ material has an intermediate chemical shift while preserving a quite-sharp *B* feature. Indeed, it has been noted by several authors that the intermediate spectra in this series (e.g., see the $x=0.5$ spectrum) are far too sharp to be a superposition of the end-point spectra, despite conventional discussions of the systems of magnetic properties in terms of dynamic Mn^{3+}-Mn^{4+} mixtures.[33] This quandary is underscored and compounded by noting that the structure of the $x=0.5$ main-edge spectrum changes only very slightly upon entering its low-temperature charge/orbital-ordered state.[34]

The Mn-K pre-edge feature spectral strength in this system has also been shown to track the Mn-valence/configuration change. The increase in the pre-edge feature strength, with increasing *x*, is illustrated in the inset of Fig. 6. The presence of three identifiable features $a1/a2/a3$ in the pre-edge of $CaMnO_3$ has been found to be characteristic of such Mn^{4+} compounds.[29] The crossover to a bimodal $a1/a2$ structure in $LaMnO_3$ is also clear in the Fig. 6 inset.

The main-edge spectra of the BCMO series shown in Fig. 7 sharply contrasts with these previous results (the differing crystal structure of the $x=0.0$ material motivates its separate consideration). While the *B* feature of the BCMO series does shift systematically to lower energy with decreasing *x*, the *B* feature also rapidly broadens and loses intensity to the region of the spectrum labeled *A* in Fig. 7. Interestingly, plotting the

B-feature energy position versus x for the (Bi, Ca) system (see Fig. 7 inset, lower right) reveals a quite good correlation with the (La, Ca) system despite the dramatically different edge-structural evolution in the two.

In Fig. 7, upper left, the pre-edge spectra of the BCMO series are shown. The spectral strength of these pre-edges decreases with decreasing x. This is consistent with the previous results on the LCMO system and with the decreasing Mn valence. The shift of intensity away from the $a2$ to the $a1$ portion of the spectrum is also consistent with that observed in the (La, Ca) system, with decreasing x and decreasing Mn valence. The formation of a particularly sharp pre-edge feature in the $BiMnO_3$ is worth noting. In previous studies by our group on defected perovskites, the appearance of such features has correlated with the formation of noncentrosymmetric MnO_6 octahedra.[29] Such local deviations from centrosymmetry would be consistent with the proposed ''ferroelectric'' distortions in $BiMnO_3$.[35]

The crystal structure of $BiMnO_3$ is highly distorted.[18] Indeed, it has been suggested that this material is in fact ferroelectrically/ferrodistortively distorted.[35] The Mn-K main-edge spectrum for $BiMnO_3$ (see Fig. 7) displayed multiple unresolved features at the edge (see the labeled features 1–4 in Fig. 7). Ti-K edge studies of the $ATiO_3$ (A=Ca, Sr, Ba, Pb) systems[36] have shown that the multiplicity and splitting of the main-edge features increase with the increasing distortion in these ferrodistortive/ferroelectric perovskites. These main-edge splittings persist far above the ferroelectric transition temperatures in these Ti-based materials, leading authors to propose reinterpretation of the ferroelectricity as an order-disorder transition of the local distortions.[37] The exceptionally large distortions in $PbTiO_3$ and $BiMnO_3$ have been attributed to the polarizability of the Pb/Bi $6s^2$ states and their incorporation into covalent bonding with the O.[18,35] The pronounced splitting of the Mn-K main-edge features is consistent with such local distortion effects.

It is tempting to associate the large modifications of the Mn main edge (upon Bi substitution into $CaMnO_3$) with disordered local distortions of the same sort that lead to the ferroelectricity in $BiMnO_3$. That such local distortions would persist at x values far from the pure ferroelectric $x=0.0$ material is not unexpected in view of the local stability of distortions in the Ti compounds at temperatures far above the ferroelectric transition.[37] To empirically test this notion, we have formed the difference spectra $\Delta\mu=[I(x)-xI(1.0)]/x$ for the BCMO series, where $I(x)$ is the Mn-K edge spectrum at a given x (Fig. 8). This procedure ''subtracts off'' a fraction x of sites assumed to remain $CaMnO_3$-like. While the authors believe that the $CaMnO_3$-like sites must in fact also evolve substantially with x, this method does provide a means of identifying subtle features in the *B*-feature broadening process.

Figure 8 displays the $CaMnO_3$ and $BiMnO_3$ spectra along with a series of $\Delta\mu$ difference spectra. As alluded to above, the subtraction procedure appears overzealous in the energy region of the $CaMnO_3$ *B*-feature peak (i.e. the ''$CaMnO_3$-like'' sites should not be x independent). Nevertheless, there are strong structures in the $\Delta\mu$ spectra at energies close to the features labeled 2 and 4 in the $BiMnO_3$

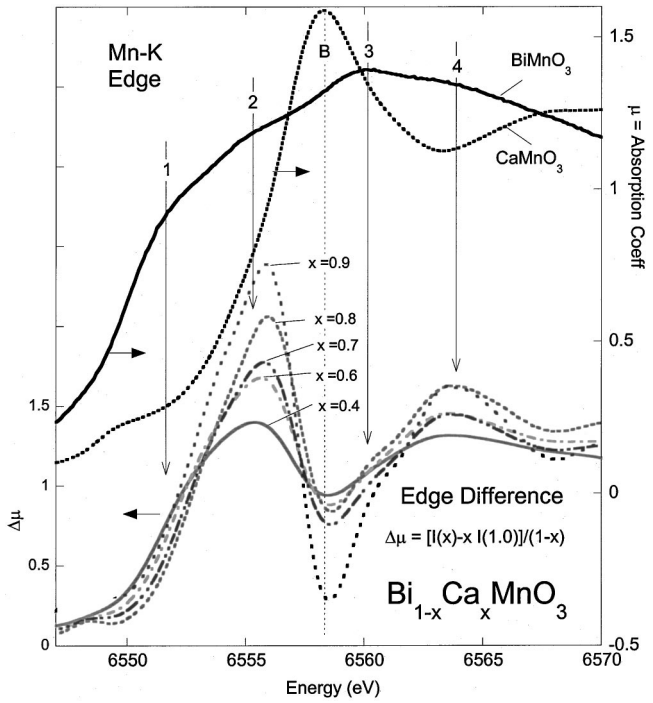

FIG. 8. The Mn-K near-edge spectra for $BiMnO_3$ and $CaMnO_3$. Lower set of curves gives the difference spectra $\Delta\mu$ for $Bi_{1-x}Ca_xMnO_3$ at $x=0.4$, 0.6, 0.7, 0.8, and 0.9. Here $\Delta\mu(E,x)=[I(E,x)-x,I(E,x=1)/(1-x)]$ was formed to approximate the spectrum of ''Bi-modified'' sites by subtracting off the fraction (x) of ''$CaMnO_3$-like'' sites and renormalizing. In doing so the authors only wish to qualitatively highlight the subtle Bi-induced local modifications and do not intend to imply the actual admixture of two such simple unmodified end-point states.

spectrum. There is also a distinct shoulder at the feature-3 energy despite the fact that it rides on the oversubtracted *B*-feature dip. At the highest concentration ($x=0.4$) the buildup of intensity in the feature-1 region is also apparent. Thus our Mn-K main-edge XAS appears consistent with the notion that Bi substitution introduces locally distorted Mn sites into the BCMO system that are similar to those that lead to the ferroelectric distortion in $BiMnO_3$.

Work by Bridges *et al.*[38] has shown modest but clear temperature dependences in the pre-edge spectra of the LCMO system in the ferromagnetic $0.2<x<0.5$ range. Recently, Qian *et al.*[34] have confirmed this effect and also discovered a different thermal dependence accompanying the onset of robust charge/orbital ordering for $0.5\leqslant x\leqslant 0.8$ in the LCMO system.

Figure 9 illustrates the variation of the Mn-K pre-edge features of the 0.6 material from above to below the charge/orbital-ordering temperature. As observed by Qian *et al.*[34] (for the La-Ca system) the spectral intensity in the lowest-energy portion of the pre-edge (the $a1$-feature region) is reduced modestly in the CO phase. The same effect was seen in the $x=0.8$ system but with a much-smaller change, presumably due to the much-weaker charge ordering near the phase's stability limit. The interpretation of these modest charge/orbital ordering induced that spectral changes are unclear at present, but two suggestions will be made here to

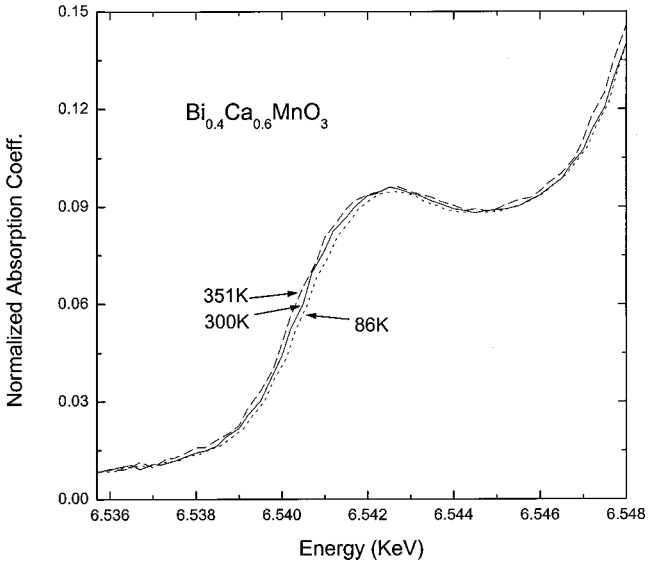

FIG. 9. Temperature-dependent pre-edge spectra of $Bi_{0.4}Ca_{0.6}MnO_3$. Note that the same trend occurs for $x=0.4$ and 0.8.

motivate theoretical calculations. A small increase in the degree of Mn^{4+} admixture accompanying the loss of ferromagnetic interactions upon entering the charge-ordered phase would at least be qualitatively consistent with the pre-edge feature change (i.e., the $a1$ feature is weakened/shifted up with increasing Mn valence). A second possibility involves the orbital component at the increased Mn^{3+} sites of the charge-ordered phase. Specifically, the static orbital alignment at these sites should be accompanied by a Jahn-Teller energy up-shift in the unoccupied e_g states. Since the $a1$ feature involves such e_g states, the charge-ordered induced degradation of the low-energy side of the $a1$ feature would be reasonable. Clearly the emergence of consistent pre-edge feature changes accompanying the phase changes in these materials should stimulate theoretical calculations of these spectral features.

F. Mn-K EXAFS

In order to compare the local structure unique of BCMO samples with LCMO samples, we have performed Mn-K-edge x-ray-absorption spectra measurements. Representative raw x-ray-absorption spectra data are shown in Fig. 10 as the inset for $x=0.9$. Note that only small changes in amplitude occur with temperature.

In Fig. 10, we show the magnitude of the Fourier transform of the EXAFS$*k^3$ spectra for selected materials in the BCMO system at 300 K. The first peak (1–2 Å) corresponds to the Mn-O bond distribution. The second (~2.5 Å) and third peaks (3.3 Å) contain the Mn-Ca/La and Mn-Mn correlations, respectively. The higher coordination peaks should also be noted. The corresponding curves for the LCMO system at 300 K are shown in Fig. 11.

The position of the first peak is related to the average Mn-O bond distance and its width is related to the spread in Mn-O bond distances. The amplitude of this peak is characterized by a Debye-Waller-factor-type reduction due to static

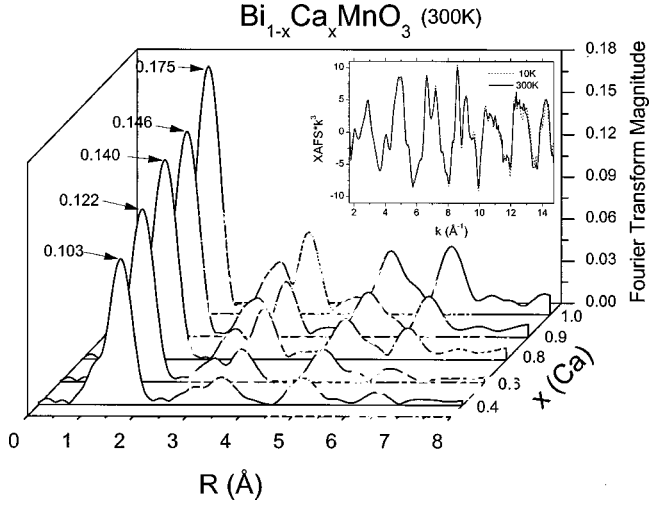

FIG. 10. Magnitude of the Fourier transform of EXAFS$*k^3$ ($2.5\ \text{Å}^{-1} \leq k \leq 12.3\ \text{Å}^{-1}$) for the system $Bi_{1-x}Ca_xMnO_3$ at 300 K. The first peak (~2 Å) corresponds to the Mn-O bond distribution. The second (~2.5 Å) and third peaks (~3.3 Å) contain the Mn-Ca/Bi and Mn-Mn correlations, respectively. The inset displays raw EXAFS$*k^3$ data for $x=0.9$ at 300 K (solid line) and 10 K (dotted line). Note that the temperature-dependent changes in amplitude are quite small.

and thermal disorder effects. Thus the Mn-O first shell in the Bi-substituted system appears to be disordered on a local scale relative to the LCMO system. The Bi-induced onset of charge/orbital-ordering correlations could contribute to this effect; however, work in our group has shown that the first Mn-O shell feature in the $La_{0.5}Ca_{0.5}MnO_3$ spectra do not show significant change upon entering the ordered state. The spectra above and below the charge-ordering temperature for the $Bi_{0.2}Ca_{0.8}MnO_3$ material also does not reveal an appreciable first-shell modification (Table I). Thus the local dis-

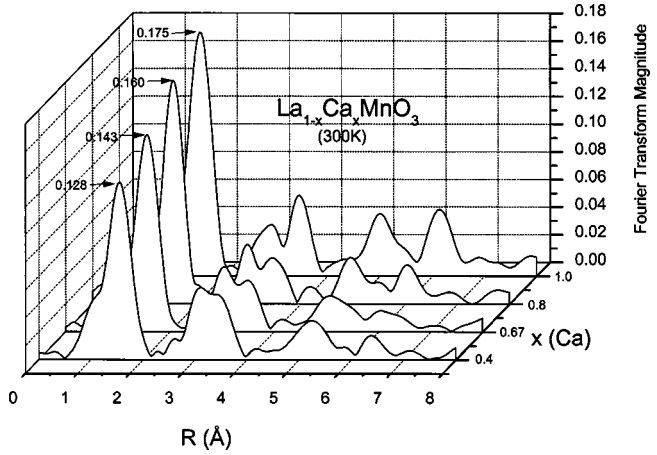

FIG. 11. Magnitude of the Fourier transform of EXAFS$*k^3$ ($2.5\ \text{Å}^{-1} \leq k \leq 12.3\ \text{Å}^{-1}$) for the system $La_{1-x}Ca_xMnO_3$ at 300 K. The first peak (~2 Å) corresponds to the Mn-O bond distribution. The second (~2.5 Å) and third peaks (~3.3 Å) contain the Mn-Ca/La and Mn-Mn correlations, respectively.

TABLE I. EXAFS derived structure at $x=0.8$, 0.9, and 1.0.

Sample	T (K)	R (Å)	σ^2	$C3$	$C4$
$Bi_{0.2}Ca_{0.8}MnO_3$	50	1.898 ± 0.002	0.0038 ± 0.0001	$-8.00\times10^{-6}\pm6.75\times10^{-6}$	$-5.02\times10^{-6}\pm4.14\times10^{-6}$
$T_{CO}=190$ K	100	1.905 ± 0.004	0.0037 ± 0.0003	$-6.00\times10^{-6}\pm6.08\times10^{-5}$	$-2.18\times10^{-7}\pm1.12\times10^{-5}$
$S_0^2=0.81$	150	1.908 ± 0.005	0.0032 ± 0.0002	$-1.10\times10^{-5}\pm7.80\times10^{-5}$	$-2.50\times10^{-5}\pm1.06\times10^{-5}$
	160	1.903 ± 0.006	0.0037 ± 0.0004	$-6.20\times10^{-5}\pm7.23\times10^{-5}$	$-6.50\times10^{-6}\pm1.08\times10^{-5}$
	170	1.905 ± 0.008	0.0038 ± 0.0004	$-5.30\times10^{-5}\pm1.07\times10^{-4}$	$-3.16\times10^{-6}\pm1.28\times10^{-5}$
	180	1.924 ± 0.008	0.0031 ± 0.0005	$2.17\times10^{-4}\pm1.11\times10^{-4}$	$-2.24\times10^{-5}\pm1.49\times10^{-5}$
	190	1.910 ± 0.005	0.0034 ± 0.0004	$1.30\times10^{-5}\pm7.10\times10^{-5}$	$-1.71\times10^{-5}\pm1.39\times10^{-5}$
	200	1.918 ± 0.007	0.0034 ± 0.0004	$1.26\times10^{-4}\pm1.07\times10^{-4}$	$-1.51\times10^{-5}\pm1.13\times10^{-5}$
	210	1.927 ± 0.010	0.0031 ± 0.0002	$2.46\times10^{-4}\pm1.40\times10^{-4}$	$-1.96\times10^{-5}\pm5.93\times10^{-6}$
	220	1.922 ± 0.011	0.0031 ± 0.0008	$1.40\times10^{-4}\pm1.69\times10^{-4}$	$-3.03\times10^{-5}\pm1.21\times10^{-5}$
	230	1.918 ± 0.008	0.0035 ± 0.0006	$1.04\times10^{-4}\pm1.12\times10^{-4}$	$-1.90\times10^{-5}\pm1.33\times10^{-5}$
	240	1.920 ± 0.003	0.0034 ± 0.00004	$1.10\times10^{-4}\pm4.75\times10^{-5}$	$-1.77\times10^{-5}\pm2.37\times10^{-6}$
	250	1.915 ± 0.003	0.0036 ± 0.0003	$4.13\times10^{-4}\pm4.88\times10^{-5}$	$-1.77\times10^{-5}\pm1.45\times10^{-5}$
	300	1.918 ± 0.007	0.0040 ± 0.0004	$9.40\times10^{-4}\pm1.04\times10^{-4}$	$-1.54\times10^{-5}\pm1.37\times10^{-5}$
$Bi_{0.1}Ca_{0.9}MnO_3$	10	1.895 ± 0.002	0.0053 ± 0.0002	$-3.40\times10^{-4}\pm1.47\times10^{-5}$	$4.47\times10^{-5}\pm2.34\times10^{-7}$
$S_0^2=0.88$	50	1.898 ± 0.008	0.0050 ± 0.0002	$-2.78\times10^{-4}\pm1.01\times10^{-4}$	$4.55\times10^{-5}\pm4.84\times10^{-6}$
	85	1.897 ± 0.005	0.0062 ± 0.0001	$-2.77\times10^{-4}\pm9.18\times10^{-5}$	$7.83\times10^{-5}\pm1.50\times10^{-5}$
	100	1.902 ± 0.012	0.0056 ± 0.0004	$-2.37\times10^{-4}\pm2.38\times10^{-5}$	$5.01\times10^{-5}\pm4.95\times10^{-6}$
	125	1.889 ± 0.015	0.0062 ± 0.0004	$-3.89\times10^{-4}\pm9.27\times10^{-5}$	$5.46\times10^{-5}\pm1.62\times10^{-5}$
	150	1.902 ± 0.002	0.0057 ± 0.0011	$-2.50\times10^{-4}\pm5.73\times10^{-5}$	$5.19\times10^{-5}\pm1.62\times10^{-5}$
	220	1.903 ± 0.003	0.0056 ± 0.0003	$-2.01\times10^{-4}\pm7.81\times10^{-5}$	$5.31\times10^{-5}\pm7.81\times10^{-5}$
	300	1.898 ± 0.003	0.0054 ± 0.0004	$-3.26\times10^{-4}\pm1.63\times10^{-5}$	$5.20\times10^{-5}\pm6.10\times10^{-6}$
$CaMnO_3$	300	1.885 ± 0.003	0.0037 ± 0.0001	$-1.79\times10^{-4}\pm5.69\times10^{-5}$	$7.91\times10^{-6}\pm2.57\times10^{-6}$
$S_0^2=0.90$					
$CaMnO_3$ XRD (Ref. 39)	300	1.899			

tortions in the Mn-O shell in the BCMO system appear to be related to the local effect of the Bi substitution and not to the longer-range charge/orbital-ordering distortions. In fact, in systematic temperature dependent on x-ray-absorption spectra measurements of the 0.8 and 0.9 systems, no significant changes in the Mn-O peak shape occur with temperature.

Detailed first-shell fits were performed on $x=0.8$ and 0.9 as well as on the $x=1.0$ and these results are reported in Table I. For high-Bi content ($x<0.8$) the spectra can not be modeled by Gaussian distributions or cumulants (expansion does not converge) because of the high level of local structural distortions. This is consistent with the very large distribution of Mn-O distances found by neutron diffraction in the $x=0$ end member $BiMnO_3$.[18]

Referring again to the BCMO results in Fig. 10, the higher-shell Mn-Bi/Ca and Mn-Mn coordination peaks are seen to be systematically reduced in amplitude with increased Bi content and in Fig. 11 they were compared to the LCMO system. This implies that the higher Bi-concentration samples are increasingly disordered. Again the potential role of charge/orbital ordering in this disordering effect must be considered. Work in our group has shown that the third-shell (Mn-Mn) feature is strongly reduced in the ordered (low-temperature) phase of the $La_{0.5}Ca_{0.5}MnO_3$ material. Thus the increasing higher-shell disorder (with increasing Bi content) in the BCMO system would appear to involve a charge/orbital-ordering contribution in addition to the local Bi-distortion contribution. Hence, local disorder induced by the Bi-$6s^2$ lone pairs stabilize charge ordering over a large-doping (x) range and suppresses the e_g hopping mediated metallic state.

V. CONCLUSION

Systematic structural, magnetic, and transport studies on the BCMO system were reported for the doping range $x \geqslant 0.4$. These measurements were correlated with x-ray absorption spectroscopy measurements. The XAS measurements clearly indicate that increasing Bi content in $CaMnO_3$ stabilizes increasing Mn^{3+} character similar to the LCMO system. However, the XAS results also indicate that very substantial local distortions about the Mn sites accompany the Bi substitution in contrast to the LCMO system. Indeed, the x-ray diffraction data reveal splittings consistent with lower-symmetry cells as Bi content increases.

The phase diagram of the BCMO system (and the magnetic and transport properties on which it is based) resembles the LCMO system in some aspects, and differs in others. The similarities to be noted are as follows. At room temperature FM interactions and enhanced electrical conductivity (decreased resistivity) are rapidly stabilized by small levels of A^{3+} substitution. FM fluctuations dominate the

high-temperature region for $x \leqslant 0.95$. A robust FM component is incorporated into the AF ground state with the maximum of this FM component correlating with the maximum conductivity enhancement near $x = 0.875$. A charge/orbital-plus AF-ordered phase onsets near $x = 0.83$, below which a line of CO ordering transition temperatures (T_{CO}) rises steeply, with decreasing x, in the phase diagrams.

A strong disparity with the LCMO system lies in the substantially more robust character of the charge-ordered state in the BCMO system. Specifically, the charge-ordering temperature rises to the 330-K range as opposed to about 250 K in the LCMO system. This remains high for x extending down to 0.4 as opposed to T_{CO} declining and the ground state converting to an FM metal below $x = 0.5$ in the LCMO system. Presumably the local Mn-O distortions stabilize the local charge/orbital-ordering process.

In general the FM-metal-to-CO-ordered insulator transition manifests the most precipitous field-sensitive conductivity change in manganite materials. Bi substitution appears to most efficiently stabilize the CO-ordering to above room temperature. Thus the use of Bi admixture in materials with high-temperature FM-metal transition temperatures may be an avenue to bring these two phenomena into competition in the room-temperature range.

ACKNOWLEDGMENTS

We are deeply indebted to Dr. T. Y. Koo (Bell Labs. and Rutgers University) for the significant effort expended in the preparation of the $BiMnO_3$ sample. We would like to thank Dr. I. Fawcett of the Rutgers University Department of Chemistry for assistance in x-ray diffraction, resistivity, and magnetic measurements. We thank also Dr. B. G. Kim for assistance with sample preparation. We are also indebted to Dr. G. Hall (Rutgers University Department of Chemistry) for assistance in XRF measurements to verify the purity of our $BiMnO_3$ high-pressure sample. We thank Dr. C. Segre of the Illinois Institute of Technology for assistance with the $BiMnO_3$ measurements at the Materials Research Collaborative Access Team (MR-CAT) at the Advanced Photon Source at Argonne National Laboratory (ANL). This research was funded by DOE Grant No. DE-FG02-97ER45665. Sample synthesis was supported by the NSF-DMR-9802513 (S-W. Cheong). X-ray absorption spectra data acquisition was performed at the National Synchrotron Light Source (Brookhaven National Laboratory), beamlines X11A, X18B, X19A, and X23A2. The $BiMnO_3$ XANES spectra were collected at the MR-CAT facility at the Advanced Photon Source (Argonne National Laboratory). Both the National Synchrotron Light Source and the Advanced Photon Source are funded by the U.S. Department of Energy.

[1] S. Jin, T. H. Tiefel, M. McCormack, R. A. Fastnachit, R. Ramesh, and L. H. Chen, Science **264**, 413 (1994); R. von Helmolt, J. Wecker, B. Holzapfel, L. Schultz, and K. Samwer, Phys. Rev. Lett. **71**, 2331 (1993); C. N. R. Rao, Anthony Arulraj, A. K. Cheetham, and Bernard Raveau, J. Phys.: Condens. Matter **12**, R83 (2000); A. P. Ramirez, *ibid.* **9**, 8171 (1997); Y. Tokura and Y. Tomioka, J. Magn. Magn. Mater. **200**, 1 (1999); C. N. R. Rao and B. Raveau, *Colossal Magnetoresistance, Charge Ordering Related Properties of Manganese Oxides* (World Scientific, Singapore, 1998); J. M. D. Coey, M. Viret, and S. von Molnar, Adv. Phys. **48**, 167 (1999).

[2] G. H. Jonker and J. H. Van Santen, Physica (Amsterdam) **16**, 337 (1950).

[3] J. H. Van Santen and G. H. Jonker, Physica (Amsterdam) **16**, 599 (1950).

[4] W. Bao, J. D. Axe, C. H. Chen, and S-W. Cheong, Phys. Rev. Lett. **78**, 543 (1997).

[5] S. Jin, M. McCormack, and T. H. Tiefel, J. Appl. Phys. **76**, 6929 (1994).

[6] G. H. Jonker, Physica (Amsterdam) **22**, 707 (1956).

[7] P. Schiffer, A. P. Ramirez, W. Bao, and S-W. Cheong, Phys. Rev. Lett. **75**, 3336 (1995).

[8] P. G. Radaelli, D. E. Cox, M. Marezio, and S-W. Cheong, Phys. Rev. B **55**, 3015 (1997).

[9] S-W. Cheong and Harold Y. Hwang, (unpublished).

[10] V. A. Bokov, N. A. Grigoryan, and M. F. Bryzhina, Phys. Status Solidi **20**, 745 (1967).

[11] H. Chiba, M. Kikuchi, K. Kusuba, Y. Muraoka, and Y. Syono, Solid State Commun. **99**, 499 (1996).

[12] H. Taguchi, Phys. Status Solidi A **88**, K79 (1985).

[13] H. Chiba, T. Atou, H. Faqir, M. Kikuchi, Y. Syono, Y. Murakami, and D. Shindo, Solid State Ionics **108**, 193 (1998).

[14] E. I. Turkevich and V. P. Plakhtii, Fiz. Tverd. Tela (Leningrad) **10**, 951 (1968) [Sov. Phys. Solid State **10**, 754 (1968)].

[15] H. L. Liu, S. L. Cooper, and S-W. Cheong, Phys. Rev. Lett. **81**, 4684 (1998).

[16] Y. Murakami, D. Shindo, H. Chiba, M. Kikuchi, and Y. Syono, Phys. Rev. B **55**, 15 043 (1997).

[17] F. Sugawara and S. Iida, J. Phys. Soc. Jpn. **20**, 1529 (1965).

[18] T. Atou, H. Chiba, K. Ohoyama, Y. Yamaguchi, and Y. Syono, J. Solid State Chem. **145**, 639 (1999); H. Chiba, T. Atou, and Y. Syono, *ibid.* **132**, 139 (1997).

[19] F. Sugawara, S. Iida, Y. Syono, and S. Akimoto, J. Phys. Soc. Jpn. **25**, 1553 (1968).

[20] E. Ohshima, Y. Saya, M. Nantoh, and M. Kawai, Solid State Commun. **116**, 73 (2000).

[21] A. Boultiff and D. Louer, J. Appl. Crystallogr. **24**, 987 (1991); J. W. Visser, *ibid.* **2**, 89 (1969).

[22] P. A. Lee, P. H. Citrin, P. Eisenberger, and B. M. Kincaid, Rev. Mod. Phys. **53**, 769 (1981); E. A. Stern, Phys. Rev. B **48**, 9825 (1993).

[23] M. Newville, P. Livins, Y. Yacoby, E. A. Stern, and J. J. Rehr, Phys. Rev. B **47**, 14 126 (1993).

[24] H. Cramér, *Mathematical Methods of Statistics* (Princeton University, Princeton, NJ, 1946), p. 186; J. Freund, R. Ingalls, and E. D. Crozier, Phys. Rev. B **39**, 12 537 (1989); G. Dalba, P. Fornasini, and F. Rocca, Phys. Rev. B **47**, 8502 (1993); G. Dalba, P. Fornasini, R. Grisenti, F. Rocca, I. Chambouleyron,

and C. F. O. Graeff, J. Phys.: Condens. Matter **9**, 5875 (1997); G. Dalba, P. Fornasini, R. Gotter, and F. Rocca, Phys. Rev. B **52**, 149 (1995); G. Dalba, P. Fornasini, R. Grisenti, F. Rocca, I. Chambouleyron, and C. F. O. Graeff, J. Phys.: Condens. Matter **9**, 5875 (1997); E. D. Crozier, J. J. Rehr, and R. Ingalls, *X-Ray Absorption* (Wiley, New York, 1988), Chap. 9, p. 373; J. M. Tranquada and R. Ingalls, Phys. Rev. B **28**, 3520 (1983); T. Yokoyama and T. Ohta, *ibid.* **55**, 11 320 (1997); J. J. Rehr and R. C. Albers, *ibid.* **41**, 8139 (1990).

[25] Grant Bunker, Nucl. Instrum. Methods **207**, 437 (1983).

[26] G. Dalba, P. Fornasini, and F. Rocca, Phys. Rev. B **47**, 8502 (1993); A. B. Edwards, D. J. Tildesley, and N. Binsted, Mol. Phys. **91**, 357 (1997).

[27] M. I. McCarthy, G. K. Schenter, M. R. Chacon-Taylor, J. J. Rehr, and G. E. Brown, Jr., Phys. Rev. B **56**, 9925 (1997).

[28] J. J. Rehr, R. C. Albers, and S. I. Zabinsky, Phys. Rev. Lett. **69**, 3397 (1992).

[29] Z. Zeng, M. Greenblatt, and M. Croft, Phys. Rev. B **59**, 8784 (1999).

[30] J. Fontcuberta, B. Martínez, A. Seffar, S. Piñol, J. L. García-Muñoz, and X. Obradors, Phys. Rev. Lett. **76**, 1122 (1996).

[31] C. M. Varma, Phys. Rev. B **54**, 7328 (1996).

[32] J. J. Neumeier and J. L. Cohn, Phys. Rev. B **61**, 14 319 (2000).

[33] G. Subias, J. Garcia, M. G. Proietti, and J. Blasco, Phys. Rev. B **56**, 8183 (1997).

[34] Q. Qian, T. A. Tyson, C.-C. Kao, M. Croft, S.-W. Cheong, and M. Greenblatt, Phys. Rev. B **62**, 13 472 (2000).

[35] N. A. Hill and K. M. Rabe, Phys. Rev. B **59**, 8759 (1999).

[36] F. Farges, G. E. Brown, Jr., and J. J. Rehr, J. Phys. IV **7**, C2-191 (1997); M. Croft (unpublished).

[37] N. Sicron, B. Ravel, Y. Yacoby, E. A. Stern, F. Dogan, and J. J. Rehr, Phys. Rev. B **50**, 13 168 (1994).

[38] F. Bridges, C. H. Booth, G. H. Kwei, J. J. Neumeier, and G. A. Sawatzky, Phys. Rev. B **61**, 9237 (2000).

[39] K. R. Poeppelmeier, M. E. Leonowicz, J. C. Scanlon, J. M. Longo, and W. B. Yelon, J. Solid State Chem. **45**, 71 (1982).